A dynamic flotation model for predictive control incorporating froth physics. Part II: Model calibration and validation

Paulina Quintanilla[a,*], Stephen J. Neethling[a], Diego Mesa[a], Daniel Navia[b], Pablo R. Brito-Parada[a]

[a] *Department of Earth Science and Engineering, Royal School of Mines, Imperial College London, South Kensington Campus, London SW7 2AZ, United Kingdom*
[b] *Departamento de Ingeniería Química y Ambiental, Universidad Técnica Federico Santa María, Campus San Joaquín, Santiago, Chile*

Abstract

Modelling for flotation control purposes is the key stage of the implementation of model-based predicted controllers. In Part I of this paper, we introduced a dynamic model of the flotation process, suitable for control purposes, along with sensitivity analysis of the fitting parameters and simulations of important control variables. Our proposed model is the first of its kind as it includes key froth physics aspects. The importance of including froth physics is that it improves the estimation of the amount of material (valuables and entrained gangue) in the concentrate, which can be used in control strategies as a proxy to estimate grade and recovery.

In Part II of this series, experimental data were used to estimate the fitting parameters and validate the model. The model calibration was performed to estimate a set of model parameters that provide a good description of the process behaviour. The model calibration was conducted by comparing model predictions with actual measurements of variables of interest. Model validation was then performed to ensure that the calibrated model properly evaluates all the variables and conditions that can affect model results. The validation also allowed further assessing the model's predictive capabilities.

For model calibration and validation purposes, experiments were carried out in an 87-litre laboratory scale flotation tank. The experiments were designed as a randomised 3^2 full factorial design, manipulating the superficial gas velocity and tailings valve position. All experiments were conducted in a 3-phase system (solid-liquid-gas) to ensure that the results obtained, as well as the behaviour of the flotation operation, are as similar as possible to those found in industrial flotation cells.

In total, six fitting parameters from the model were calibrated: two terms from the equation for overflowing bubble size; three parameters from the bursting rate equation; and the number of pulp bubble size classes. After the model calibration, simulations were performed to validate the predictions of the model against experimental data. The validation results revealed good agreement between experimental data and model predictions of important flotation variables, such as pulp level, air recovery, and overflowing froth velocity. The high accuracy of the predictions suggests that the model can be successfully implemented in predictive control strategies.

Keywords: Froth flotation, flotation control, flotation modelling, model calibration, model validation, model predictive control

1. Introduction

Model Predictive Control (MPC) is attracting widespread interest in fields such as mineral processing. One of the main aspects of MPC is the availability of a dynamic model of the process that is accurate enough – yet simplified – to make predictions on important variables. However, for most mineral processing unit operations, developing accurate, simplified dynamic models is a challenge. This challenge is particularly significant for the froth flotation, as it is a multiphase process with inherent instability.

Despite the importance of the froth phase in the overall performance of a flotation cell, only few studies have included it in their models for predictive control, such as those found in Bascur (1982); Zaragoza and Herbst (1989); Putz and Cipriano (2015); Tian et al. (2018). A deeper discussion of these studies is found in Part I of this paper, while an extensive literature review on modelling for flotation control can be found in Quintanilla et al. (2021). The froth models included into control strategies by Zaragoza and Herbst (1989); Putz and Cipriano (2015); Tian et al. (2018) are rather oversimplified as kinetic models, and/or did not take into account important aspects of the froth physics, such as bubble coalescence, bursting rate, air recovery, and liquid motion, to name a few.

The need to incorporate froth physics into control strategies is crucial as froth stability has a significant impact on the overall performance of flotation cells (Neethling and Brito-Parada, 2018). Air recovery has been used to measure froth stability in previous studies (Hadler and Cilliers, 2009; Hadler et al., 2010, 2012; Shean et al., 2017; Neethling and Brito-Parada, 2018). It is defined as the fraction of air entering the cell that does not burst. It has been demonstrated that operating at air flowrates at which a peak in air recovery (PAR) is found favours optimal overall flotation performance. The optimal flotation performance translates into an improvement in the concentrate grade, recovery or both (Hadler and Cilliers, 2009). Air recovery can be measured online if sufficient instrumentation is available on site. The model equation to calculate air recovery (α) is:

$$\alpha = \frac{v_f l_{lip} h_{over}}{Q_{air,in}}. \tag{1}$$

The air flowrate ($Q_{air,in}$) is essentially the same as $j_g A_{cell}$, where j_g is the superficial gas velocity and A_{cell} is the cross-sectional area of the cell. The overflowing froth velocity (v_f) can be measured by image analysis using cameras located at the top of the flotation cell, for example. The froth height (h_{over}) is the height over

*Corresponding author
Email address: p.quintanilla18@imperial.ac.uk (Paulina Quintanilla)

the cell lip, and it can be measured by using optical lasers located above the overflowing launder. A further explanation of these measurements is presented in Section 2.3, as air recovery was measured online in the experiments performed for model validation in this paper. In this work, we present a novel dynamic model for flotation control that includes froth stability. The development of a dynamic flotation model along with a sensitivity analysis of the parameters and simulations of important variables were presented in Part I of this paper. It was concluded that there were seven fitting parameters that need to be calibrated with the available data. Two of these parameters correspond to the equation for overflowing bubble size:

$$d_{b,\text{ froth out}} = \left(nC\tau_f + d_{b,int}^n\right)^{1/n}, \tag{2}$$

where n and C are the parameters to be calibrated. The term τ_f is the mean froth residence time, while the term $d_{b,int}$ corresponds to the interfacial bubble size. The equation used for estimating the interfacial bubble size is presented in Part I of this paper. Unlike the model equation for bubble size at the top of the froth presented by Oosthuizen et al. (2021) (discussed in Part I of this paper), here we present a model for the overflowing bubble size at the lip length, based on the model developed by Neethling and Cilliers (2003) for bubble coalescence.

In order to incorporate froth stability in the model, we related air recovery to the rate at which bubbles burst at the surface of the froth (ie. the bursting rate). The bursting rate (v_b) has been demonstrated to have a dependency on the superficial gas velocity (j_g) as follows (Neethling and Brito-Parada, 2018):

$$v_b = a + bj_g + cj_g^2, \tag{3}$$

where a, b and c are parameters to be calibrated. The bursting rate at the top of the froth has been identified to have a quadratic trend (Neethling and Brito-Parada, 2018), depending on the operating conditions in the flotation cell and the Peak in Air Recovery (PAR). If no PAR is found, a linear relationship with j_g is established, i.e. the parameter c will not be statistically significant; hence it will be set to zero.

By considering the definition of air recovery, we can establish a relationship between the bursting rate at the top of the froth, v_b, and the interfacial gas velocity, v_g^*, as follows:

$$\alpha^* = \frac{v_g^* - v_b}{v_g^*}. \tag{4}$$

The interfacial gas velocity (v_g^*) was described in Part I as the contribution of the total upward gas velocity $v_{g,\text{out pulp}}^{total}$, and the change in pulp height with time, ($\frac{dh_p}{dt}$), as presented in Eq. 5. The interfacial velocity should not be confused with the superficial gas velocity (j_g), which being defined as the total air flowrate entering the cell divided by the cross-sectional area of the cell.

$$v_g^* = \frac{dh_p}{dt} + v_{g,\text{ out pulp}}^{\text{total}}. \tag{5}$$

Additionally, unlike the study presented by Oosthuizen et al. (2021), in which froth recovery was not defined and it was rather replaced by α; we have incorporated a simplified equation to calculate froth recovery factor ($R_{f,i}$). The froth recovery factor is used to calculate the mass reported in the concentrate due to true flotation. It is defined as the fraction of the material that enters into the froth attached to the bubbles that reports to the concentrate, rather than dropping back into the pulp (Finch and Dobby, 1991; Neethling, 2008). Although it is difficult to measure, it can be estimated using Eq. 6, which is a simple theoretical approximation developed in Neethling (2008).

$$R_{F,i} = \begin{cases} \left(\frac{\alpha^*(1-\alpha^*)v_g^*}{v_{\text{set},i}}\right)^{\frac{f}{2}} \left(\frac{d_{b,\text{ int}}}{d_{\text{bfroth}}}\right)^f & \text{if } \alpha < 0.5 \\ \left(\frac{v_g^*}{v_{\text{set},i}}\right)^{\frac{f}{2}} \left(\frac{d_{b,\text{ int}}}{d_{\text{bfroth}}}\right)^f & \text{if } \alpha \geq 0.5 \end{cases} \tag{6}$$

The term f is yet another important parameter of the model. It is a constant value between 0 and 1 which represents the fraction of material that becomes detached from the bubble surfaces during coalescence (Neethling, 2008). The other terms in Eq. 6 are: air recovery α^* (Eq. 4), the interfacial gas velocity v_g^*, the particle settling velocity $v_{set,i}$, the interfacial bubble size $d_{b,int}$, and the overflowing bubble size $d_{b,froth}$ (Eq. 2). The equations to determine v_g^*, $v_{set,i}$, and $d_{b,int}$, are presented in Part I of this paper.

The seventh parameter of the model we developed in Part I corresponds to the number of bubble size classes in the pulp phase: K. This parameter is present in the equations used to calculate the dynamic gas holdup, gas volume in the pulp, and upward gas velocity. Although the accuracy of the model increases as K increases, it was demonstrated in Part I that the elapsed time for solving the model also increases significantly. There is, thus, a trade-off in this parameter as the elapsed time is crucial for the implementation of the model into MPC strategies.

The purpose of Part II of this series is to present the calibration and validation of the model defined in Part I. A large set of experiments were carried out in an 87-litre laboratory-scale flotation tank, as described in Section 2. Five parameters of the model were calibrated as detailed in Section 3.1 and relevant variables were validated against experimental data, as shown in Section 3.2. This is the first study that presents calibration and validation of a dynamic model for control purposes incorporating froth physics.

2. Materials and methods

In order to calibrate and validate the proposed model presented in Part I of this paper, a series of experiments were carried out in a laboratory-scale flotation tank using a 3-phase system (solid-liquid-gas). All experiments were performed in triplicates, under the same dosage of frother and collector, as well as maintaining the solid fraction constant at 20% w/w. A detailed explanation of the experimental setup, materials and methods used in this set of experiments are described in the following subsections.

2.1. Experimental setup: Laboratory-scale flotation tank

All experiments were conducted in an 87 litre laboratory-scale flotation tank at Imperial College London. Details of this flotation tank are given in Mesa and Brito-Parada (2020). Air was injected from the centre of the base of the tank, through a single nozzle. The pulp was agitated using a rotor impeller (see Figure 1a), based on the OK rotor from Outokumpu/Outotec (Burgess, 1997; Grau and Heiskanen, 2005). The impeller was 3D printed in graphite-reinforced nylon due to its mechanical properties such as wear resistance, high compressing strength, and resistant to alkali chemicals (Kang and Chung, 2003; Pan et al., 2012; Mesa and Brito-Parada, 2020). The tank also has a stator of 22 blades (see Fig. 1b), which was 3D printed in ABS (acrylonitrile butadiene styrene). The reason of the selection of ABS is that it is strongly resistant to chemical corrosion and physical impacts at a low cost (Aliheidari et al., 2017; Mesa and Brito-Parada, 2020). A schematic of the tank, rotor and stator is presented in Fig. 1. The dimensions of the tank that were used for the model calibration (Section 3.1) and validation (Section 3.2) are presented in Table 1. These are the same dimensions as those used for the sensitivity analysis and simulations in Part I of this paper.

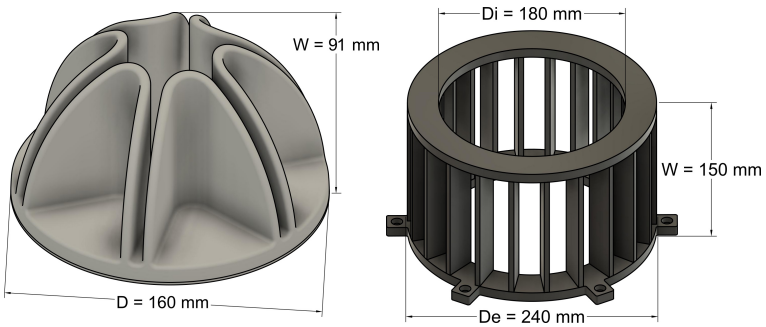

(a) Rotor

(b) Stator

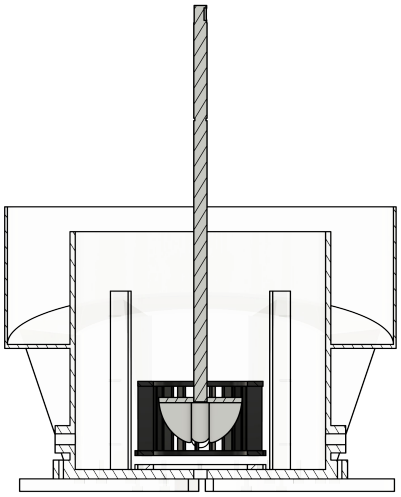

(c) Laboratory-scale flotation tank

Figure 1: Schematic of the 87-litre laboratory-scale flotation tank used for model validation. Adapted from Mesa and Brito-Parada (2020).

Table 1: Flotation cell dimensions in the experimental setup.

Dimension	**Symbol**	**Value**	**Unit**
Cross-sectional area of the cell	A_{cell}	0.18	m^2
Volume of the cell	V_{cell}	0.087	m^3
Total height of the cell	h_T	0.48	m
Lip length	l_{lip}	1.51	m

In the laboratory-scale flotation tank, the concentrate and tailings flowrates are recirculated, as shown in Figure 2). The instruments and equipment associated to this flotation rig are reported in Table 2.

Slurry is prepared in a sump tank (T-2) before starting the operation. A Rushton impeller allowed the solids to be suspended in the sump (T-2) and the chemical reagents to properly mix with the slurry. The slurry and chemical reagents preparation are detailed in sub-section 2.2.

The flotation tank was fed from the sump tank (T-2) through a gear pump (P-1). Froth depth below the overflowing lip was measured using a Guided Radar Level (LI-1), which was connected to a PLC. The overflowing froth was collected in the launder and drained into the sump tank (T-2). Measurements of overflowing froth velocity were captured through four digital cameras (DC 1-4) that were equidistantly installed over the tank. The cameras were connected to a computer to analyse the images using a block-matching image analysis program developed at Imperial College London (Norori-McCormac et al., 2017). Froth height above the overflowing lip was measured using two equidistant laser level sensors (LI 2 and 3), which were connected to a PLC.

The tailings flowrate were measured online using a magnetic flowmeter (FI-1), which was also connected to a PLC. The tailings flow into the sump (T-2) were recirculated back to the flotation tank (T-1). The tailings valve was manually set in terms of its % of opening. A further explanation of the tailings valve operation and manipulation is given in sub-section 2.3.

Air flowrate was injected at the bottom of the flotation tank (T-1) using a mass flow controller (FIC-1). The controller allowed to set a desired set point for the superficial gas velocity, j_g, via controlling the air flowrate valve. The impeller speed was also controllable via an inverted drive (WIC-1) which allowed to set the speed between 0 to 1000 rpm. For the purposes of model validation we used a standard value of 450 rpm as reported in Mesa and Brito-Parada (2020).

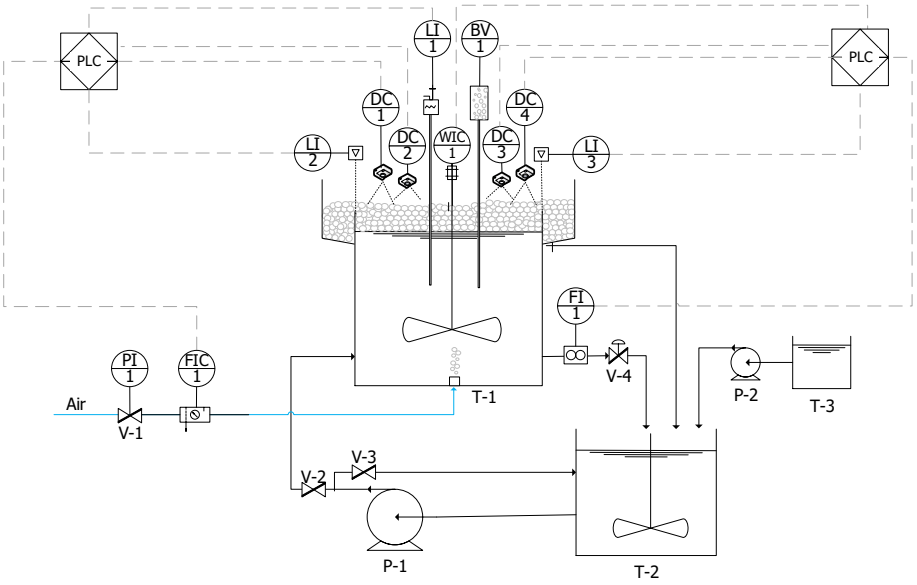

Figure 2: P&ID of the laboratory-scale flotation tank. Table 2 shows the tag names nomenclature.

Table 2: Available instruments and equipment in the experimental rig. The Tag column corresponds to the nomenclature used in the P&ID (Fig. 2).

Instrument	Tag	Measurement	Connected to PLC	Indicator	Controller
Bubble viewer	BV-1	Bubble size in the pulp	No	No	No
Digital camera	DC-1/2/3/4	Overflowing velocity	Yes	Yes	No
Magnetic flowmeter	FI-1	Tailings flowrate	Yes	Yes	No
Mass flow controller	FIC-1	Air flowrate	Yes	Yes	Yes
Guided radar level sensor	LI-1	Froth depth	Yes	Yes	No
Laser distance sensor	LI-2/3	Froth height	Yes	Yes	No
Pressure gauge	PI-1	Air pressure	No	Yes	No
Air control valve	V-1	N/A	Yes	No	Yes
Feed manual valve	V-2	N/A	No	No	No
Feed manual valve	V-3	N/A	No	No	No
Tailings manual valve	V-4	N/A	No	No	Manually
Torque controller	WIC-1	Impeller speed	Yes	Yes	Yes
Equipment	**Tag**	**Type**	**Range / Dimensions**	**Units**	
Slurry feed pump	P-1	Bare shaft pump	2 to 20	lpm	
Reagents pump	P-2	Peristaltic	0 to 4	lpm	
Flotation tank	T-1	Cylindrical, baffled tank	87	litres	
Sump tank	T-2	Plastic tank	125	litres	
Reagents preparation tank	T-3	Plastic	5	litres	

2.2. Materials and reagents

The solids used for all experiments were glass beads sourced from Key Abrasives Ltd, UK. The glass beads had a particle size between 75 and 150 μm. The chemical composition of the solids is mainly SiO_2 (silica). The slurry used for the experiments was, therefore, a single-species system. This is the same used in previous experiments, as those described in Morrison (2017); Norori-McCormac et al. (2017); Mesa et al. (2020). The single-species system can be used to evaluate the effects on changes in operating conditions (Norori-McCormac et al., 2017), such as air and tailings flowrate, which is ideal for the model validation purpose.

A slurry of 20% w/w solid content was prepared by mixing 25 kg of solids and 100 litres of tap water (London, UK) in the sump (T-2) and agitating for at least 5 minutes. The chemical reagents used for these experiments were Dowfroth 250 (DF250, provided by Nasaco), which was used as frother, and Tetradecyltrimethylammonium bromide (TTAB, from Sigma Aldrich), which was used as collector. First, the collector was added to the slurry in the sump at an initial dosage of 16g of TTAB per tonne of solids (i.e. 16 ppm in mass). The slurry and collector were agitated for another 5 minutes at 450 RPM. Then, the frother was

added to the sump at an initial dosage of 4 μl of frother per litre of water (i.e. 4 ppm in volume) (Mesa et al., 2020). Another 5 minutes of agitation were allowed to ensure well-mixed conditions.

Since the experiments were run continuously for at least 3 hours per test, TTAB (collector) addition was needed to maintain froth stability, as reported in Norori-McCormac et al. (2017) and Mesa et al. (2020). Therefore, TTAB was dosed continuously to the tank at a rate of 50 mg per hour (Mesa et al., 2020) using a peristaltic pump (P-2 from Fig. 2).

2.3. Experimental methodology

The instrumentation available in the experimental rig allowed to measure a number of variables at dynamic state, which are presented in Table 3. It must be noted that online data for air recovery (from Eq. 1) at dynamic state was also collected because both the overflowing froth velocity (v_f) and the froth height over the lip (h_{over}) were measured at dynamic states.

Table 3: Flotation variables measured in the experiments. The symbols correspond to the nomenclature of the model proposed in Part I of this paper.

Variable	**Symbol**	**Range**	**Unit**	**Type of measurement**
Air flowrate	Q_{air}	$5.5 \times 10^{-4} - 1.6 \times 10^{-3}$	$m^3 s^{-1}$	Dynamic and steady states
Tailings flowrate	$Q_{tailings}$	$6.67 \times 10^{-5} - 2 \times 10^{-4}$	$m^3 s^{-1}$	Dynamic and steady states
Height over the lip	h_{over}	0.01 - 0.02	m	Dynamic and steady states
Bubble size in the pulp	$d_{b,pulp}$	$7 \times 10^{-4} - 7 \times 10^{-3}$	m	Steady state
Overflowing froth velocity	v_f	0.01 - 0.04	ms^{-1}	Dynamic and steady states
Pulp height	h_p	0.3 - 0.48	m	Dynamic and steady states
Position of the tailings valve (open)	O_v	25-50	%	Steady state

The experiments were carried out as a randomised 3^2 full factorial design, i.e. changing 2 variables, each at three levels. These two variables were the superficial gas velocity j_g and the tailings valve position. The tests were run varying j_g between 0.5, 0.7 and 0.9 $[cms^{-1}]$ and the tailings valve position was varied manually between 25%, 37.5% and 50% opening. Collector dosage was maintained constant at 16 ppm in mass.

The values for j_g were selected based on previous experiments in the same experimental rig used in Mesa and Brito-Parada (2020); Mesa et al. (2020). The tailings valve position was manually manipulated to generate changes in the tailings flowrate ($Q_{tailings}$). The valve has a physical indicator that corresponded to one eighth of its full range (i.e. each turn corresponded to an extra 12.5% opening).

Figure 3 shows the evolution of tailings flowrate against valve position. Error bars represent the standard deviation of the experimental data. The changes on the valve position were selected after running preliminary experiments. For valve positions smaller than 25%, the tailings inevitably blocked the tubes and, therefore, it was not possible to run the flotation rig. A valve opening in the range 25-50% was sufficient for our purpose,

as it allowed the tailings to flow between 4 to 12 litre per minute (lpm). A valve opening above 50% was not useful for model validation purposes since, as can be seen in the figure, the changes in the tailings flowrate were very small, and therefore did not generate sufficient changes in the operating conditions. This is explained by the fact that it is a nonlinear valve.

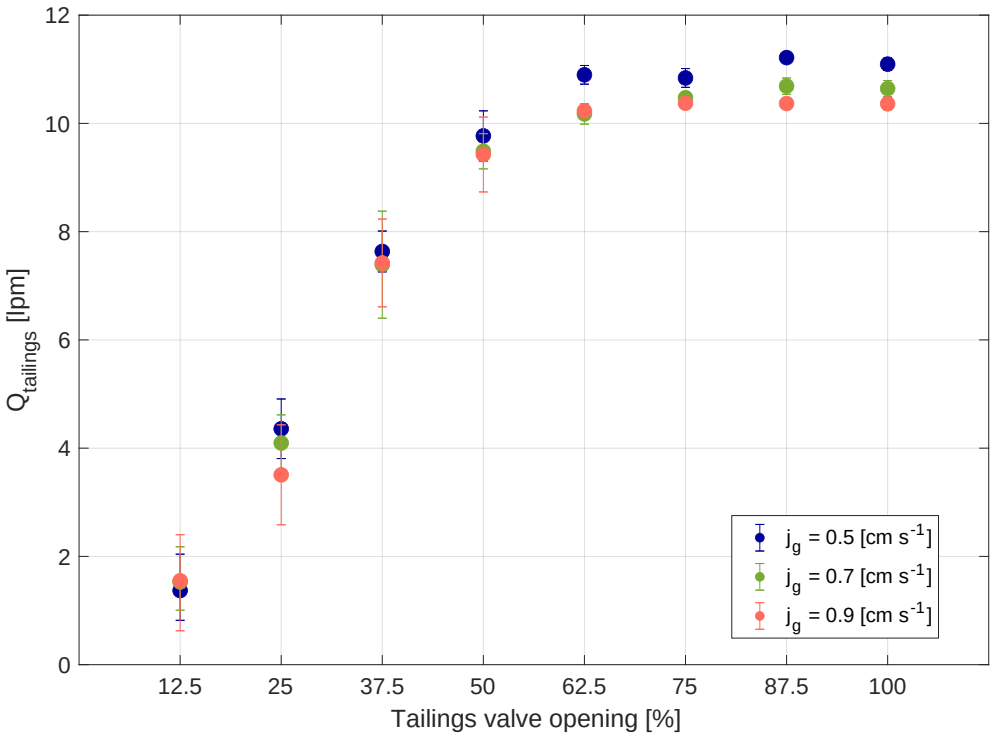

Figure 3: Tailings flowrate ($Q_{tailings}$) in the experimental system as a function of the position of the valve [%] and the superficial gas velocity (j_g). Error bars represent the standard deviation of the experimental data.

The operating conditions for the feed are presented in Table 4. These values were used for model calibration and validation in the next section. All experiments were run in triplicate for further statistical analysis.

Table 4: Feed properties in the experiments, which were performed for model calibration and validation (Sections 3.1 and 3.2).

Feed properties	**Symbol**	**Value**	**Unit**	**Source**
Feed flowrate	Q_{feed}	$5 \times 10^{-5} - 2.5 \times 10^{-4}$	$m^3 s^{-1}$	Estimated (See Section 3)
Water density	ρ_{water}	1000	kgm^{-3}	Assumption
Water viscosity	μ_{water}	10^{-3}	$Pa\ s$	Assumption
Solids density	ρ_{solids}	2500	kgm^{-3}	Supplied by manufacturer
Gravity	g	9.81	ms^{-2}	Assumption
Particle size	$d_{P,i}$	75×10^{-6}	m	Supplied by manufacturer
Solid fraction	Φ	0.2	-	Experimental setup

Bubble size distribution in the pulp was measured using a bubble viewer apparatus. This equipment was designed by Mesa and Brito-Parada (2020) based on the design proposed by Hernandez-Aguilar et al. (2002). For each experimental condition, 300 photographs were taken, at a rate of 1 frame per second. This means that at least 3000 bubbles per condition were considered for analysis to ensure robust results (Quinn et al., 2007; Kracht et al., 2008; Quinn et al., 2014; Mesa and Brito-Parada, 2020). A Canon EOS 80D camera with a Canon EF-S 60 mm f/2.8 macro lens, shutter speed bulb 1/2500 was used to obtain the photographs. Following 5 minutes of stabilisation time, the photographs were taken when the experiment reached steady-state. Once the experiments finished, the photographs were analysed off-line using a Matlab routine to determine the bubble size distribution. The bubble size classes (K), an important parameter in the model proposed, were also determined. Concentrate samples were obtained when the system reached steady-state (after 5 minutes) for all experiments. Each sample was taken during a 10 seconds period, in triplicate, which allowed the estimation of the concentrate flowrate. This concentrate flowrate estimate was then used to calibrate two model fitting parameters, as detailed in Section 3.1. The samples were weighed before and after being placed in an oven to be dried for 48 hours. The sampling was carried out to obtain a proxy for metallurgical recovery and grade for the single-species system. Mass pull and solids content were used for this purpose, respectively (Norori-McCormac et al., 2017; Morrison, 2017; Mesa et al., 2020).

3. Results and discussion

Experimental data from the laboratory-scale flotation circuit described in the previous section (Section 2) were collected to calibrate and validate the dynamic model proposed in Part I of this paper. Since the feed flowrate could not be measured in the experiments, this variable was estimated through the implementation of a Control Vector Parametrization (CVP) algorithm.

The CVP algorithm is used to convert the optimisation problem into a nonlinear programming problem by parametrization of control profiles (Schlegel et al., 2005). In this case, the Q_{feed} was discretised at different

time intervals having an initial guess for the first optimisation. This variable was defined as piecewise constant [Q_{feed_1} ... Q_{feed_N}]. N is the number at which the total simulation time (500 seconds) was divided by, i.e. N = total time/Δt. The optimisation started for N = 2, with an initial guess of $Q_{feed_1} = 9.5[lpm]$ and $Q_{feed_2} = Q_{tailings_j}$, where j is the experiment number. The tailings flowrate for the experiments were between 4.5 and 10 [lpm], as can be seen in Figure 3. The results from the first optimisation were used as initial values for the next optimisation at N = 4. This process was performed repeatedly until N = 32.

The dynamic optimisation problem was implemented in Matlab 2021 using a function to find the minimum of a constrained optimisation problem (*fmincon*), which uses a Sequential Quadratic Programming (SQP) method. The model presented in Part I of this paper can be classified as a Differential and Algebraic Equation (DAE) problem. The differential equations of the DAE problem were solved using the function *ode15s* in Matlab. The cost function for the optimisation was to minimise the normalised difference between the pulp height experimental (h_p^{exp}) and predicted (h_p^{pred}) for each set of experiments:

$$\min_{Q_{feed}} \sum_{j=1}^{9} \sum_{i=0}^{tf} \left(\frac{h_{p_i}^{exp} - h_{p_i}^{pred}}{h_{p_i}^{exp}} \right)_j^2 \tag{7}$$

s.t.

$$2 \leq Q_{feed_j} \leq 15[lpm] \tag{8}$$

The pulp height predicted was calculated, as detailed in Part I of this paper, using Eq. 9. The definition of total pulp height (h_p) considers the contribution from the liquid and gas phases in the pulp. It was calculated by integrating the dynamic model for gas holdup and "gas free" pulp height. The differential equation obtained for pulp height was:

$$\frac{dh_p}{dt} = \frac{1}{A_{cell}} \left(Q_{feed} - Q_{pulp,out} \right) \left(\frac{1}{1 - \sum_{k=1}^{K} \varepsilon_0^k} \right) + \frac{h_0}{\left(1 - \sum_{k=1}^{K} \varepsilon_0^k \right)} \sum_{k=1}^{K} \frac{d\varepsilon_0^k}{dt}, \tag{9}$$

where A_{cell} is the cross-sectional area of the flotation cell, Q_{feed} and $Q_{tailings}$ are the feed and tailings flowrates, respectively; h_0 is the gas free pulp height, and ε_0^k is the gas holdup of the bubble size class k.

Regarding the CVP optimisation, the boundary conditions for Q_{feed} were chosen by means of the tailings flowrate range measured at laboratory scale. The final results from the optimisation for each Q_{feed_j} is shown in Figure 4. As it can be seen, these results are in line with the values obtained in the tailings flowrate at steady state (see Figure 3), which is a good indicator of the estimation for Q_{feed}.

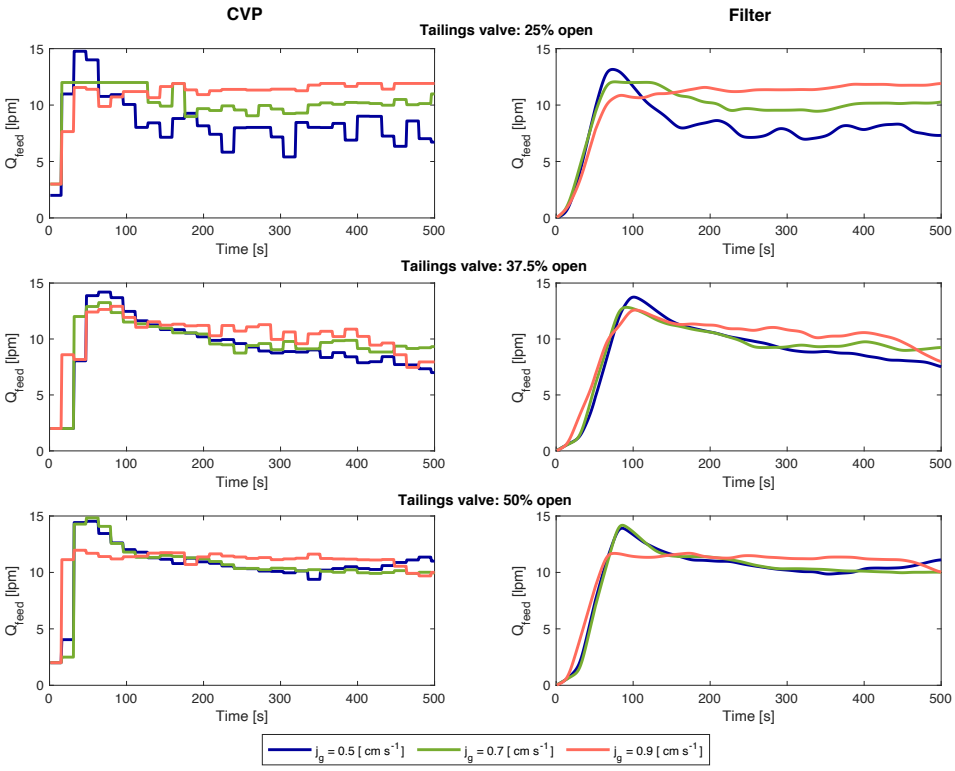

Figure 4: Left: Feed flowrate (Q_{feed}) estimated using Control Vector Parametrization. The results presented here are the final results of the dynamic optimisation problem at N = 32. Right: Feed flowrate (Q_{feed}) filtered using a rational transfer function, with a moving-average filter.

The results from the nonlinear optimisation with CVP were filtered using a rational transfer function in order to have smoother behaviour of Q_{feed}. The filter uses a moving-average filter, with a windows size of 31 [s]. A detailed explanation of the rational transfer function function can be found in Oppenheim et al. (1999), while the full description of the Matlab function used in this study (*filter* function) is found in the Matlab documentation (MATLAB, 2021).

3.1. Model calibration of fitting parameters

The fitting parameters of the proposed model in Part I of this paper were calibrated using experimental data obtained in the laboratory-scale flotation circuit. These parameters are: the exponential (n) and constant (C) values for bubble size at the overflowing lip (Eq. 2); constants values a, b and c for bursting velocity (Eq. 3); and the number of bubble size classes (K). The model calibration was performed to determine the value of these six unknown parameters by minimising the difference between the experimental data set and the model prediction.

3.1.1. Parameters for overflowing bubble size (n and C):

The overflowing bubble size (Eq. 2) can be calculated by means of the residence time in the froth (τ_f) and the bubble size in the interface ($d_{b,int}$). The most appropriate way to calibrate the parameters would be by comparing the simulated results with actual measurements of the bubble size in the overflowing lip ($d_{b,\text{froth out}}$). However, this type of measurement is not straightforward (Wang and Neethling, 2006). The nonlinear data-fitting problem was instead solved by comparing the experimental and predicted concentrate flowrate, which is inversely proportional to the overflowing bubble size.

The experimental concentrate flowrates were obtained by weighing the concentrate samples, as explained in section 2.3. The predicted concentrate flowrate was calculated as detailed in Part I of this paper, using the following model (Neethling et al., 2003):

$$Q_{conc} = \begin{cases} \frac{A_{cell} v_g^{*2} \lambda_{out} (1-\alpha^*)\alpha^*}{k_1} & \text{if } \alpha < 0.5 \\ \frac{A_{cell} v_g^{*2} \lambda_{out}}{4k_1} & \text{if } \alpha \geq 0.5 \end{cases}, \tag{10}$$

where A_{cell} is the cell cross-sectional area, v_g^* is the interfacial gas velocity (from Eq. 5), λ_{out} is the length of the Plateau border, α^* is the froth air recovery, and k_1 is a physical parameter that is calculated as in Eq. 11:

$$k_1 = \frac{\rho_{\text{pulp}} g}{3 C_{PB} \mu_{\text{pulp}}}, \tag{11}$$

where ρ_{pulp} is the pulp density and μ_{pulp} is the pulp density. The term C_{PB} represents the drag coefficient that is assumed to be constant and equal to 50.

This concentrate flowrate is inverse to the overflowing froth bubble size $d_{b,\text{froth out}}$ (from Eq. 2) as λ_{out} is calculated as shown in Eq. 12, where the bubbles are assumed to be Kelvin cells (i.e. $k_\lambda = 6.815$) (Neethling et al., 2003):

$$\lambda_{out} = \frac{k_\lambda}{d^2_{b\text{froth out}}}. \tag{12}$$

The fitting procedure was implemented in Matlab, using a nonlinear least-squares solver (*lsqnonlin* function). The objective function was to minimise the least-square of the normalised difference between the experimental and predicted concentrate flowrate (Q_{conc}) at steady state.

$$\sum_{i=1}^{9} \left(\frac{Q^{pred}_{\text{conc},i} - Q^{exp}_{\text{conc},i}}{Q^{exp}_{\text{conc},i}} \right)^2 \tag{13}$$

s.t.

$$\begin{aligned} 1 \leq n \leq 2 \\ C \geq 0 \end{aligned} \tag{14}$$

where i corresponds to the number of different conditions of the experiments – i.e. 9 conditions in total, as a combination between changes in superficial gas velocity: j_g = 0.5, 0.7 and 0.9 cms^{-1} and the tailings valve opening at 25%, 37.5% and 50%. The optimisation was subject to the constrains presented in Eq. 14. Limits for n had to be set between 1 and 2, as reported in Neethling and Cilliers (2003). The parameter C was set as a positive number. In order to avoid overfitting, the experimental data set was divided into two different data sets with the same amount of data points (50/50) such as the first data set was used for the model calibration, and the second data set was used for model validation (see Figure 5). Table 5 shows the values of n and C obtained from the nonlinear least-square solver, along with their 95% confidence interval.

Table 5: Calibrated parameters for Eq. 2, which is used to calculate the overflowing bubble size.

Parameter	**Value**	**Units**	**95% confidence intervals**
n	1.00	–	[0.409, 1.591]
C	6.38×10^{-4}	ms^{-1}	$[6.17 \times 10^{-5}, 6.59 \times 10^{-5}]$

In order to validate the model, the experimental overflowing bubble sizes, $d^{exp}_{b,\text{froth out}}$, were estimated using Eq. 2, assuming that the interfacial bubble size ($d_{b,int}$) was equal to the pulp phase bubble size (measured via image analysis as described in Section 2.3). The froth residence time was calculated in the same way as presented in Part I of this paper:

$$\tau_f = \frac{h_f}{v_g^*}. \tag{15}$$

Here, we used experimental dynamic data for the froth height (h_f), and replaced the interfacial gas velocity (v_g^*) by the superficial gas velocity (j_g).

Figure 5 presents the dynamic overflowing bubble size (diameters) after the optimisation for model calibration. The shaded envelopes correspond to the 95% confidence intervals of the experimental data, which were calculated by measuring the standard deviation of each experimental set as they were performed in triplicates. Prediction intervals (black dashed lines in the figure) were calculated in order to estimate the interval at which a future observation will fall. The sensitivity analysis showed in Part I of this paper revealed that the parameters n and C are strongly nonlinear respect to the estimation of overflowing bubble size and concentrate flowrate. These non-linearities, besides the fact that Eq. 2 is not an explicit function of time, make the calculation of the prediction intervals not straightforward and difficult to obtain. However, it is well known that 95% of the observation will fall approximately within (plus/minus) two times the standard error of estimation (S). S is calculated as in Eq. 16, representing the average difference between the observed values and the model predictions, using the units of the dependent variable. Smaller values of

S are better because it means that the observations are closer to the model predictions.

$$\mathrm{S} = \sqrt{\frac{\sum \left(y^{pred} - y^{exp}\right)^2}{N-2}}, \tag{16}$$

In this case, y^{pred} is the overflowing bubble size calculated with Eq. 2, and y^{exp} is the experimental overflowing bubble size. The term $(N-2)$ represents the degrees of freedom of the model, which is the total number of observations or data points minus two parameters (n and C). The standard error of estimate obtained for all cases are between 2.81×10^{-4} and 8.42×10^{-4} [m], which are one order of magnitude less than the actual value of overflowing bubble sizes.

The model calibration performed here seems to be acceptable as the objective function considered the minimisation of the concentrate flowrate. However, it should be noted that the experimental concentrate flowrate was measured only at steady-state and therefore the dynamic prediction could benefit from including measurements of the concentrate flowrate in the experimental methodology.

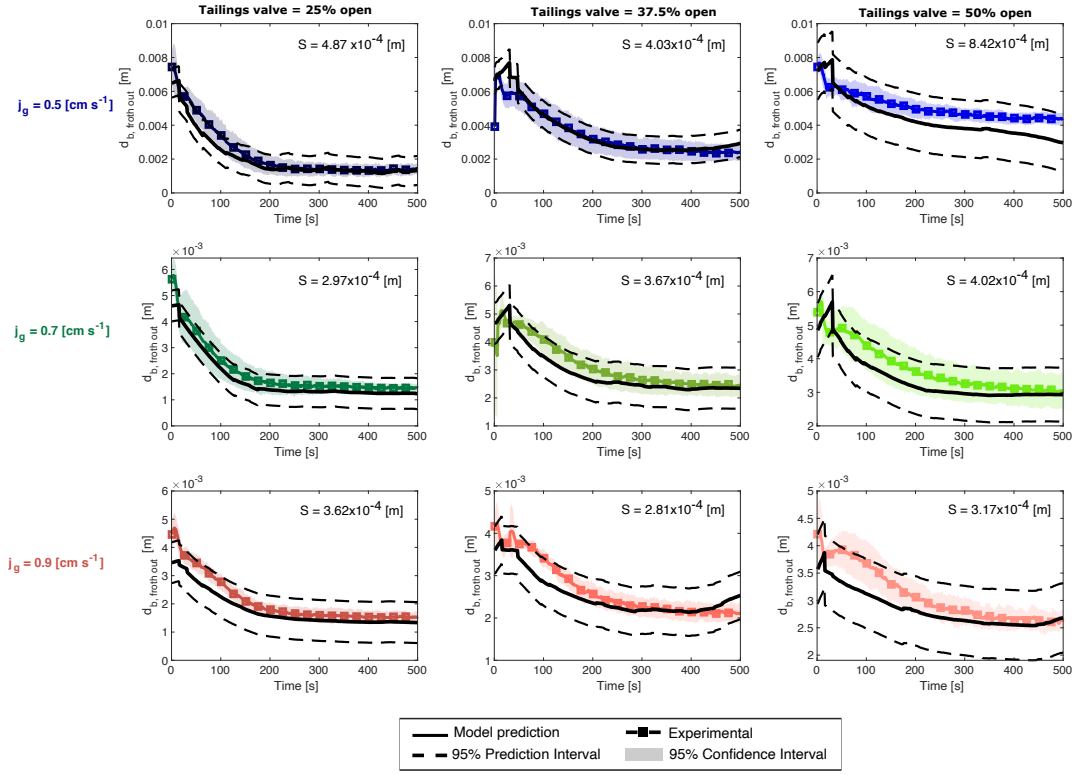

Figure 5: Dynamic experimental and predicted overflowing bubble size calculated from Eq. 2 after the model calibration. The squared lines correspond to the experimental overflowing bubble size, while the black solid lines are the predicted pulp height. The shaded envelopes represent the 95% confidence interval of the estimated experimental data. The black dashed lines are the prediction intervals calculated as two times the standard error of estimate (S). There are 9 different conditions in total, which are the combination of the range of $j_g = 0.5$ (blue), 0.7 (green) and 0.9 (red) $[cms^{-1}]$, and the different positions of the tailings valve opening used in the experiments: 25% (first column), 37.5% (second column) and 50% (third column).

As it can be also seen in Figure 5, the curves for the experimental and predicted $d_{b,\text{froth out}}$ are very similar in most cases, having essentially the same dynamics. Besides, the predicted overflowing bubble sizes are within the expected average size range, falling between 0.1 and 0.8 cm. Although a slight discrepancy can be seen at the steady state value for one condition ($j_g = 0.5$ $[cms^{-1}]$ and tailings valve opening at 50%); these results, undoubtedly, are promising for future use of the model into predictive control strategies because the model is capable of predicting the dynamic trajectory of $d_{b,\text{froth, out}}$.

3.1.2. Parameters of the busting rate equation (a, b, and c):

The bursting rate (v_b) can be defined by means of the superficial gas velocity (j_g) as was shown in Eq. 3, which indicates a quadratic relationship between v_b and j_g. However, note that the quadratic relationship

will appear only when a Peak in Air Recovery (PAR) is found (Neethling and Brito-Parada, 2018).

The calibration of the parameters of bursting rate was performed at steady-state as j_g displays very fast dynamics. The experimental bursting rate was indirectly measured as proposed by Neethling and Brito-Parada (2018), based on the same methodology used to measure the air recovery from a flotation cell (Hadler and Cilliers, 2009; Norori-McCormac et al., 2017):

$$v_b = j_g - \frac{v_f l_{\text{lip}} h_{\text{over}}}{A_{\text{Cell}}}. \tag{17}$$

The term $\frac{v_f l_{\text{lip}} h_{\text{over}}}{A_{\text{Cell}}}$ is the gas overflowing as unburst bubbles. Thus, the difference between both terms is the gas lost through the bursting, v_b. As described in Section 2.3, the overflowing froth velocity v_f and the froth height h_{over} were measured using image analysis and optical lasers, respectively. The procedure to measure these variables is further explained in Section 2.

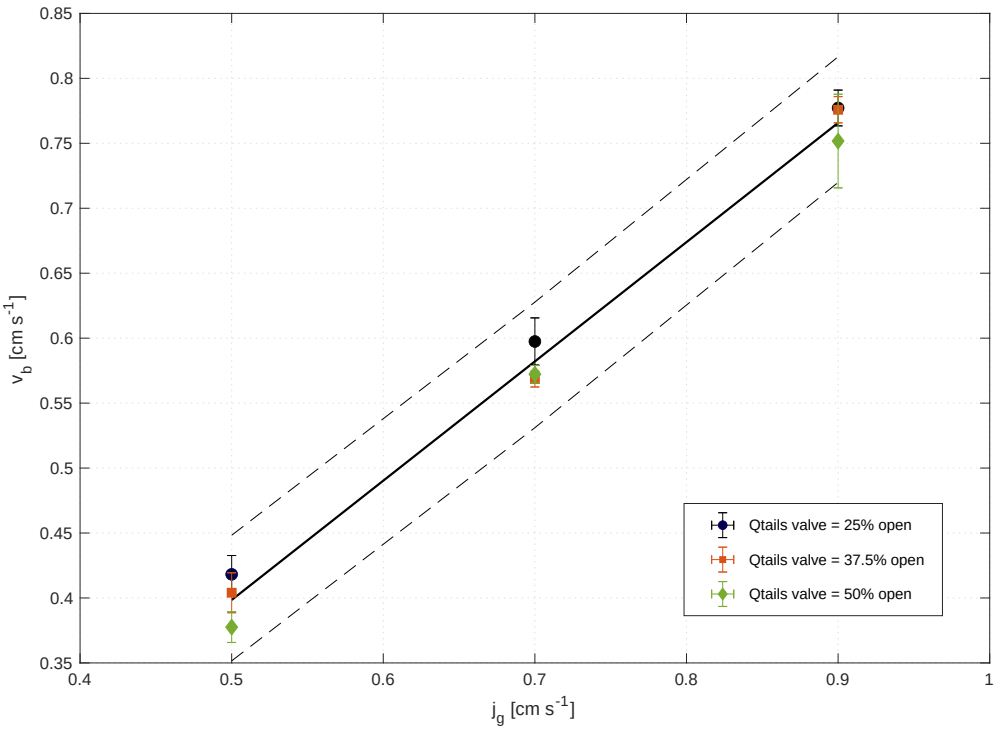

Figure 6: Relationship between the bursting rate and the superficial gas velocity entering into the flotation cell (j_g), for each tailings flowrate condition. Data is shown with their 95% confidence interval. The solid line correspond to the Eq. 3 calculated with the coefficients shown in Table 6. The dashed lines are the prediction intervals at 95% confidence.

Figure 6 presents the trend in bursting rate with a linear increase in bursting rate with the superficial gas

velocity, as expected, since a Peak in Air Recovery was not clearly reached in this particular experimental data set.

Since the slope and the intersect do not drastically change for the different tailings flowrate cases, single values of the parameters a, b were calculated among their confidence bounds at 95%. As can be seen in Table 6, both parameters are statistically significant. Moreover, the goodness of fit of this calibration are: Squared Sum Error (SSE) = 1.8 $\times 10^{-7}$, $R^2_{adj} = 0.99$; and the Root Mean Squared Error (RMSE) = 0.0157, meaning that this fit is useful for prediction.

Table 6: Calibrated parameters for Eq. 3, which is used to calculate the bursting rate (v_b) as a function of superficial gas velocity into the cell (v_g).

Parameter	**Value**	**Units**	**95% confidence intervals**
a	-6.21×10^{-4}	ms^{-1}	$[-1.17 \times 10^{-3}, -6.41 \times 10^{-5}]$
b	0.9208	–	[0.8434, 0.9982]

3.1.3. Number of bubble size classes in the pulp (K):

The number of bubble size classes in the pulp (K) needs to be defined properly in order to have accurate, and yet fast, results. In fact, while a large number of bubble size classes implies an increase in accuracy, the computational power needed to solve the model will also increase. Since this model was developed to be implemented into predictive control strategies, a trade-off between computational time and accuracy must be taken into consideration.

The parameter K depends on the bubble size data available. In the experiments carried out for this paper, we had a large set of bubble size measurements that were performed using a Bubble Sizer, as described in Section 2.3. Figure 7 shows the accuracy of the dynamics of the pulp height for one of the twelve conditions carried out in the experiments.

The pulp height was chosen to evaluate the accuracy for two reasons: (1) it directly depends on the gas hold up, which is a function of bubble size classes, and (2) it is a measured variable in the experiments, therefore, a comparison between predicted and experimental data could be performed. As it can be seen in the box plot of Figure 7, there is a huge difference between the predicted and experimental pulp height for $K < 4$, with an error of almost six times bigger than those for $K \geq 5$. A slight increase in the error for $K > 5$ might be caused by the methodology used for estimating the feed flowrate using Control Vector Parametrization, as shown in the beginning of this section, since the optimisation was performed using $K = 5$. While the accuracy clearly improves for larger K, the sensitivity analysis performed in Part I of this paper showed that the elapsed time to solve the DAE problem increases up to 30% in comparison with the elapsed time at $K = 5$.

To sum up, Table 7 presents the values of all parameters of the proposed dynamic model. As it can be seen,

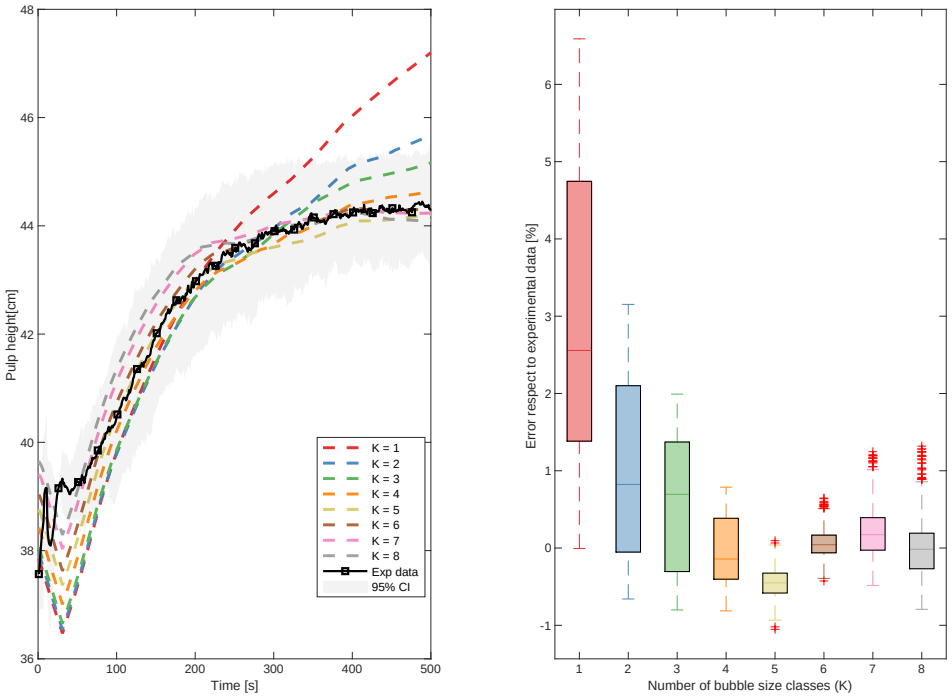

Figure 7: Left: Predicted and experimental pulp height dynamics for the central operating condition ($j_g = 0.7$ $[cms^{-1}]$ and tailings valve at 37.5% opening), for different values of K (number of bubble size classes in the pulp). The dashed lines correspond to the simulations performed using different values of K. The squared black solid line correspond to the experimental data. The shaded envelope corresponds to the 95% confidence interval of the experimental data. Right: Errors in pulp height predictions against the number of bubble size classes.

6 out of 7 fitting parameters were calibrated (n, C, a, b, c and K), while the exponential factor of the froth recovery model (f) was taken from literature. Note that the detailed development of the model proposed is presented in Part I of this series, whereas a summary table of all the model equations is presented in the supplementary material of Part II.

3.2. Model validation

Simulations were performed to validate and identify the accuracy of the proposed dynamic model. All simulations were performed using the values of the parameters shown in Table 7, feed properties shown in Table 4, cell dimensions shown in Table 1, and the estimated Q_{feed} shown in Figure 4. The validation focuses on the evaluation of the model performance regarding three measured variables: pulp height (h_p, from Eq. 9), air recovery (α^*, from Eq. 4), and overflowing froth velocity (v_f, from Eq. 18). Simulations

Table 7: Parameters of the dynamic model presented in Part I of this paper.

Parameter	**Symbol**	**Value**	**Unit**	**Source**
Exponential value for bubble size in the froth	n	1	-	Fitted
Constant value for bubble size in the froth	C	6.38×10^{-4}	ms^{-1}	Fitted
Fitting parameter for bursting rate	a	-6.06×10^{-4}	ms^{-1}	Fitted
Fitting parameter for bursting rate	b	0.9182	-	Fitted
Fitting parameter for bursting rate	c	0	-	Fitted
Number of bubble size classes	K	5	-	Fitted
Exponential factor for froth recovery	f	0.8	-	Neethling and Cilliers (2008)
Floatability	P_i	2.8×10^{-4}	-	Hu et al. (2013)
Viscous drag coefficient	C_{PB}	50		Neethling et al. (2003)
Peclet number	Pe	0.15	-	Lee et al. (2005)
Lambda constant	k_λ	6.815	-	Neethling et al. (2003)

for the interfacial gas velocity (v_g^*, from Eq. 5) are also shown here to analyse and compare its dynamics with the typical value of superficial gas velocity j_g.

3.2.1. Pulp height:

The experimental data of pulp height was compared with the predicted pulp height, calculated from Eq. 9. As mentioned previously, the definition of total pulp height (h_p) considers the contribution from the liquid and gas phases in the pulp. In part I of this paper, a detailed explanation of the derivation of this model is presented. Figure 8 presents the pulp height dynamics for different conditions in j_g and tailings valve positions. In terms of the dynamic model, the change in tailings valve means that changes in the tailings flowrate were performed. As it can be seen from this figure, the model is capable of accurately predicting the pulp height in all conditions. Better accuracy is achieved for higher j_g, which is a good indicator as industrial flotation cells typically operate at slightly higher j_g values.

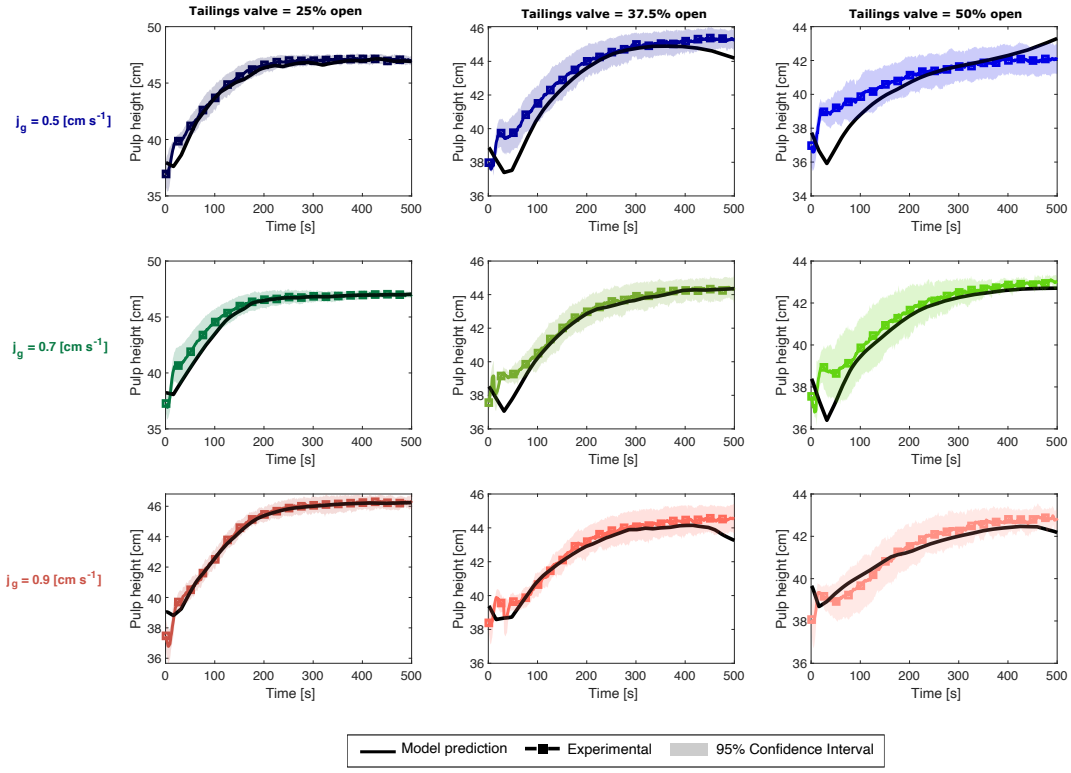

Figure 8: Model validation for pulp height after the model calibration. The shaded envelopes represent the 95% confidence interval of each experiment. The squared lines correspond to the experimental pulp height, while the black solid lines are the predicted pulp height. There are 9 different cases in total, which are the combination of the range of $j_g = 0.5$ (blue), 0.7 (green) and 0.9 (red) $[cms^{-1}]$, and the different positions of the tailings valve opening used in the experiments: 25% (first column), 37.5% (second column) and 50% (third column).

This model for pulp level prediction was also tested by Shean et al. (2018). However, they used a water-reagents-air system only (i.e. with no solids). Whereas their study exhibited slight differences in the changes in pulp level, being usually overestimated, our model validation reveals an appropriate match between the experimental data and the predictions. This could be explained by the differences in the systems used (our experiments were performed in a three-phase system: solid-liquid-gas), as well as due to the assumptions on bubble size distribution. Unlike the empirical model for bubble size distribution used by Shean et al. (2018), we have incorporated experimental data of bubble sizes, which were measured via image analysis as explained in Section 2.3.

Finally, it should be noted that, while prediction intervals were estimated for the validation of $d_{b,\text{froth out}}$

and v_b, in this case we have not presented the prediction intervals for pulp height. The reason is that the model used for h_p (Eq. 9) is completely phenomenological; therefore, it does not have any parameter to be calibrated. The absence of fitting parameters implies that the calculation of prediction intervals for h_p is conceptually wrong. It must be emphasised that a phenomenological model is always desirable as it can be used for a wide range of operating conditions (Quintanilla et al., 2021). This is particularly useful for model predictive control as pulp height is a typical controlled variable in flotation.

3.2.2. Air recovery:

The experimental data of air recovery was compared with the predicted air recovery (α^*) calculated from Eq. 4. This comparison is presented in Figure 9, where the squared lines are the experimental data, and the black solid lines are the predicted air recovery. The confidence interval of the experiments is also shown as shaded envelopes, calculated with the standard deviation of the experiments that were carried out in triplicates for each condition. The black dashed lines are the prediction intervals.

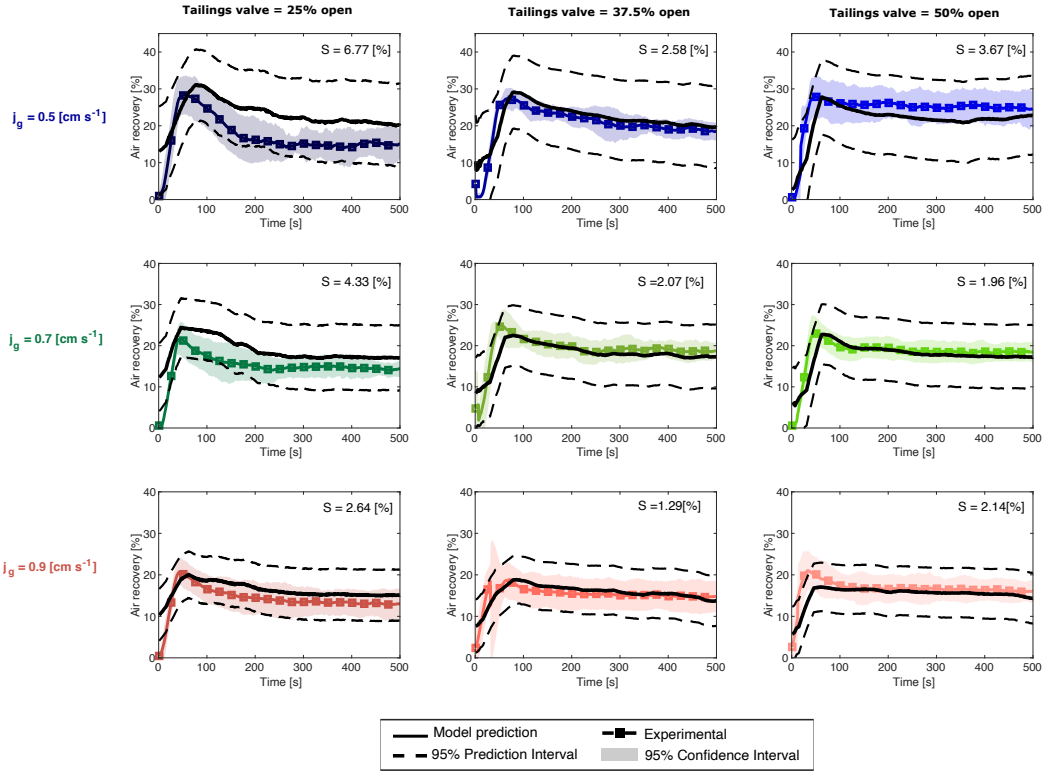

Figure 9: Model validation for air recovery after the model calibration. The shaded envelopes represent the 95% confidence interval of each experiment. The squared lines correspond to the experimental air recovery, while the black solid lines are the predicted air recovery using Eq. 4. S is the standard error of estimate, calculated as Eq. 16. There are 9 different cases in total, which are the combination of the range of $j_g = 0.5$ (blue), 0.7 (green) and 0.9 (red) $[cms^{-1}]$, and the different positions of the tailings valve opening used in the experiments: 25% (first column), 37.5% (second column) and 50% (third column).

The prediction intervals could be estimated because, as it can be seen in Eq. 4, α^* depends on v_b from Eq. 3, which has two fitted parameters (an intercept a, and a slope b). In the sensitivity analysis presented in Part I of this paper, it was concluded that a is considerably more sensitive than b. In fact, the analysis revealed that while α^* would change up to $\pm 50\%$ from its nominal value for changes of $\pm 24\%$ in a, changes as small as $\pm 1.5\%$ in α^* were found for the same changes in b. These results then allow us to estimate the prediction intervals by simulating α^* within the confidence intervals for a, maintaining b at its nominal value from Table 6.

As can be clearly seen in Figure 9, the dynamic values of the air recovery yield an acceptable agreement with the experimental data. The standard error of estimate shown on the upper right corner of each plot, which were calculated using Eq. 16, reveals that the average difference between the observed values and the model

prediction will fall within 1.29% to 6.77%, depending on the operating condition. What is more important here, though, is that the model has the ability to follow the trend in the air recovery dynamics. This ability is crucial for the model to be successfully implemented into predictive control strategies. Comparing all the values of the standard error of estimate, S, it can be seen that the prediction improves as j_g increases. It appears that for larger j_g values the model would have an even better agreement with the experimental data. This outcome further supports the idea of implementing the proposed model at industrial scale, as usually the j_g are close to the higher value in the experiments (0.9 cms^{-1}).

3.2.3. Overflowing froth velocity:

The overflowing froth velocity over the lip v_f was measured and analysed as described in Section 2. Equation 18 was used to estimate this variable, which is as a function of concentrate flowrate (from Eq. 10), the cell lip length (l_{lip}, from Table 1), and the slurry content in the froth ϵ (Neethling and Cilliers, 2008). The model equation for the slurry content ϵ and further details of the model are presented in Part I of this paper.

$$v_f = \frac{Q_{\text{conc}}}{\epsilon l_{\text{lip}}\, h_{\text{over}}}. \tag{18}$$

Figure 10 presents the experimental data (squared lines) with their respective confidence interval (shaded envelopes), as well as the v_f predicted (black solid lines) for each conditions. Similarly with the pulp height, in this case the prediction intervals cannot be calculated because this is a fully phenomenological model; thus, it does not have any fitting parameter, which makes it conceptually impossible to estimate the prediction intervals.

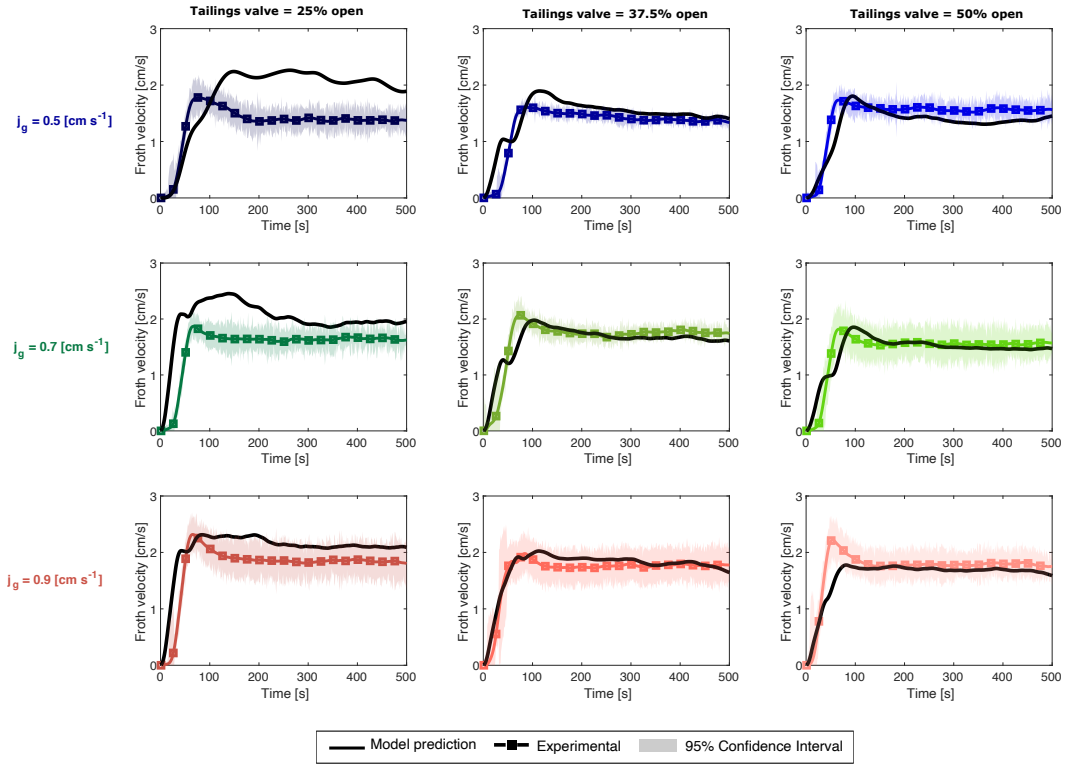

Figure 10: Model validation for overflowing froth velocity using Eq. 18. There are 9 different cases in total, which are the combination of the range of $j_g = 0.5$, 0.7 and 0.9 $[cms^{-1}]$, and the different positions of the tailings valve: 25%, 37.5% and 50% opening used in the experiments.

As can be clearly seen from the figure, the model predictions show good agreement with the experimental data sets. Slight differences are found for the three conditions at which tailings valve are 25% open. This could be explained by the fact that the froth depth in this condition is shallower than valve openings at 37.5% and 50%, which could have a rather negative effect in froth stability. However, despite these differences, the results suggest that the predictions obtained from Eq. 18 follow the dynamic trend for overflowing froth velocity in all cases. This is particularly powerful for predictive control purposes because it implies that this will enable the use of v_f as a controlled variable, as a proxy for controlling air recovery. As discussed previously, it has been demonstrated that air recovery is strongly linked with optimal flotation performance, and therefore, it would be convenient to include air recovery into control strategies in future work.

3.2.4. Interfacial gas velocity:

The interfacial gas velocity was defined in Part I of this paper as the contribution of changes in pulp height (from Eq. 9) and the gas velocity out of the pulp. Figure 11 presents the dynamics of the interfacial gas velocity, v_g^*, simulated using Eq. 5. It is observed that the value of v_g^* converges to the value of j_g in all cases. The dynamics is clearly slower than what is expected for j_g because v_g^* is greatly influenced by the changes of pulp height in time, which tend to stabilise from approximately t =200 seconds.

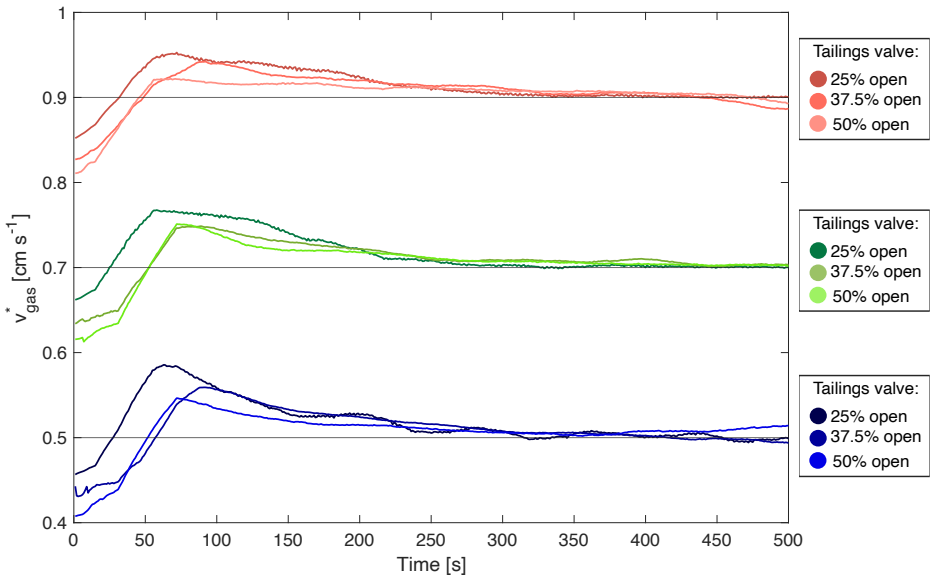

Figure 11: Model validation for interfacial gas velocity, calculated using 5. The horizontal lines at 0.5, 0.6 and 0.9 $[cms^{-1}]$ mark the value of j_g for that particular experiment. There are 9 different cases in total, which are the combination of the range of j_g = 0.5, 0.7 and 0.9 $[cms^{-1}]$, and the different positions of the tailings valve: 25%, 37.5% and 50% opening used in the experiments.

Figure 11 also shows that the highest peaks in v_g^* are achieved when the tailings valve is open 25%, i.e. for shallow froth depths. This can be explained by what can be seen in Figure 8, where the dynamics of pulp height is faster when the tailings valve is at 25% open. The advantage of including pulp-froth interface models, such as v_g^* from Eq. 5, is that it allows adding a dynamic term to the equation for air recovery (α^* from Eq. 4); hence, it enables more precise dynamic state predictions. An accurate prediction is significantly important for the implementation of effective predictive controllers.

4. Conclusions

Prior work has demonstrated that froth stability has a major impact on flotation performance. However, in terms of models for flotation control, few attempts have been made to include the froth phase. In fact,

most of the available literature shows that the froth phase has either been oversimplified or just neglected, and rather focuses on models for the pulp phase.

In this paper, we have presented the calibration and validation of the dynamic model introduced in Part I of this series, which incorporates froth physics. The model calibration and validation were performed using experimental data from an 87-litre laboratory scale flotation tank. Measurements of important flotation variables such as pulp level (dynamic), air recovery (dynamic), and pulp bubble size distribution (steady-state) were performed while manipulating the air and tailings flowrates (through their respective control valves). These flowrates are the typical manipulated variables in flotation control. The experiments in each operating condition were carried out in triplicates for further statistical analysis.

Six fitting parameters of the proposed model were calibrated using experimental data. The 95% confidence intervals of each fitting parameter, except for the number of bubble size classes (K), were also calculated. The fitting parameters n and C of the equation of overflowing bubble size (Eq. 2) were calibrated by minimising the sum of the squares of the difference between the experimental and predicted concentrate flowrate. From this optimisation, the value obtained for n was 1 ± 0.591 and for C was $6.17 \times 10^{-4} \pm 2.1 \times 10^{-5}$. The three fitting parameters of the bursting rate (v_b) equation (Eq. 3) were calibrated, obtaining a equal to $-6.06 \times 10^{-4} \pm 4.9 \times 10^{-4}$, b equal to 0.9182 ± 0.0776, and c was not statistically significant, and therefore it was set to zero. Finally, the fitting parameter K was set to 5 because it was the best value that presented a good trade-off between elapsed time to solve the model and accuracy.

In general, the results of the validation of the dynamic model demonstrated high accuracy in the predictions. The validation results also revealed that the model can follow the trend of important variables such as pulp level, air recovery, and overflowing froth velocity. This ability of predicting the trend is crucial for the implementation of our model into predictive control strategies. Furthermore, having models of the froth phase for MPC will allow detailed predictions and therefore better control strategies to maximise the amount of valuable metal recovered. Future work will focus on the experimental implementation of the model proposed here into predictive control strategies.

5. Acknowledgements

Paulina Quintanilla would like to acknowledge the National Agency for Research and Development (ANID) for funding this research with a scholarship from "Becas Chile". The Society of Chemical Industry is also greatly acknowledged for the support granted by the SCI Messel Scholarship 2020.

References

Aliheidari, N., Tripuraneni, R., Ameli, A., Nadimpalli, S., 2017. Fracture resistance measurement of fused deposition modeling 3D printed polymers. Polymer Testing 60, 94–101. doi:10.1016/j.polymertesting.2017.03.016.

Bascur, O.A., 1982. Modelling and computer control of a flotation cell. University of Utah, Salt Lake City .

Burgess, F.L., 1997. OK100 tank cell operation at Pasminco - Broken Hill. Minerals Engineering 10, 723–741. doi:10.1016/s0892-6875(97)00051-4.

Finch, J.A., Dobby, G.S., 1991. Column flotation: A selected review. Part I. International Journal of Mineral Processing doi:10.1016/0301-7516(91)90062-N.

Grau, R.A., Heiskanen, K., 2005. Bubble size distribution in laboratory scale flotation cells. Minerals Engineering 18, 1164–1172. doi:10.1016/j.mineng.2005.06.011.

Hadler, K., Cilliers, J.J., 2009. The relationship between the peak in air recovery and flotation bank performance. Minerals Engineering doi:10.1016/j.mineng.2008.12.004.

Hadler, K., Greyling, M., Plint, N., Cilliers, J.J., 2012. The effect of froth depth on air recovery and flotation performance. Minerals Engineering 36-38, 248–253. URL: http://dx.doi.org/10.1016/j.mineng.2012.04.003, doi:10.1016/j.mineng.2012.04.003.

Hadler, K., Smith, C.D., Cilliers, J.J., 2010. Recovery vs. mass pull: The link to air recovery. Minerals Engineering 23, 994–1002. URL: http://dx.doi.org/10.1016/j.mineng.2010.04.007, doi:10.1016/j.mineng.2010.04.007.

Hernandez-Aguilar, J.R., Gomez, C., Finch, J., 2002. A technique for the direct measurement of bubble size distributions in industrial flotation cells, in: Proceedings of the 34th Annual Meeting of the Canadian Mineral Processors, pp. 389–402.

Hu, W., Hadler, K., Neethling, S.J., Cilliers, J.J., 2013. Determining flotation circuit layout using genetic algorithms with pulp and froth models. Chemical Engineering Science 102, 32–41. doi:10.1016/j.ces.2013.07.045.

Kang, S.C., Chung, D.W., 2003. Improvement of frictional properties and abrasive wear resistance of nylon/graphite composite by oil impregnation. Wear 254, 103–110. doi:10.1016/S0043-1648(02)00302-2.

Kracht, W., Gomez, C.O., Finch, J.A., 2008. Controlling bubble size using a frit and sleeve sparger. Minerals Engineering 21, 660–663. doi:10.1016/j.mineng.2007.12.009.

Lee, H.T., Neethling, S.J., Cilliers, J.J., 2005. Particle and liquid dispersion in foams. Colloids and Surfaces A: Physicochemical and Engineering Aspects 263, 320–329. doi:10.1016/j.colsurfa.2004.12.064.

MATLAB, 2021. 1-D digital filter - MATLAB filter - MathWorks United Kingdom. URL: https://uk.mathworks.com/help/matlab/ref/filter.html#buagwwg-2.

Mesa, D., Brito-Parada, P.R., 2020. Bubble size distribution in aerated stirred tanks: Quantifying the effect of impeller-stator design. Chemical Engineering Research and Design 160, 356–369. doi:10.1016/j.cherd.2020.05.029.

Mesa, D., Morrison, A.J., Brito-Parada, P.R., 2020. The effect of impeller-stator design on bubble size: Implications for froth stability and flotation performance. Minerals Engineering 157, 106533. doi:10.1016/j.mineng.2020.106533.

Morrison, A., 2017. Tank design modifications for the improved performance of froth flotation equipment. Imperial College London .

Neethling, S.J., 2008. Simple approximations for estimating froth recovery. International Journal of Mineral Processing doi:10.1016/j.minpro.2008.09.007.

Neethling, S.J., Brito-Parada, P.R., 2018. Predicting flotation behaviour âĂŞ The interaction between froth stability and performance. Minerals Engineering 120, 60–65. URL: https://doi.org/10.1016/j.mineng.2018.02.002, doi:10.1016/j.mineng.2018.02.002.

Neethling, S.J., Cilliers, J.J., 2003. Modelling flotation froths. International Journal of Mineral Processing 72, 267–287. doi:10.1016/S0301-7516(03)00104-2.

Neethling, S.J., Cilliers, J.J., 2008. Predicting air recovery in flotation cells. Minerals Engineering 21, 937–943. doi:10.1016/j.mineng.2008.03.011.

Neethling, S.J., Lee, H.T., Cilliers, J.J., 2003. Simple relationships for predicting the recovery of liquid from flowing foams and froths. Minerals Engineering 16, 1123–1130. doi:10.1016/j.mineng.2003.06.014.

Norori-McCormac, A., Brito-Parada, P.R., Hadler, K., Cole, K., Cilliers, J.J., 2017. The effect of particle size distribution on froth stability in flotation. Separation and Purification Technology 184, 240–247. doi:10.1016/j.seppur.2017.04.022.

Oosthuizen, D.J., le Roux, J.D., Craig, I.K., 2021. A dynamic flotation model to infer process characteristics from online measurements. Minerals Engineering 167, 106878. doi:10.1016/j.mineng.2021.106878.

Oppenheim, A.V., Schafer, R.W., Buck, J.R., 1999. Discrete-Time Signal Processing. Upper Saddle River, NJ: Prentice-Hall.

Pan, B., Zhang, S., Li, W., Zhao, J., Liu, J., Zhang, Y., Zhang, Y., 2012. Tribological and mechanical investigation of MC nylon reinforced by modified graphene oxide. Wear 294-295, 395–401. doi:10.1016/j.wear.2012.07.032.

Putz, E., Cipriano, A., 2015. Hybrid model predictive control for flotation plants. Minerals Engineering 70, 26–35. doi:10.1016/j.mineng.2014.08.013.

Quinn, J.J., Kracht, W., Gomez, C.O., Gagnon, C., Finch, J.A., 2007. Comparing the effect of salts and frother (MIBC) on gas dispersion and froth properties. Minerals Engineering 20, 1296–1302. doi:10.1016/j.mineng.2007.07.007.

Quinn, J.J., Sovechles, J.M., Finch, J.A., Waters, K.E., 2014. Critical coalescence concentration of inorganic salt solutions. Minerals Engineering 58, 1–6. doi:10.1016/j.mineng.2013.12.021.

Quintanilla, P., Neethling, S.J., Brito-Parada, P.R., 2021. Modelling for froth flotation control: A review. Minerals Engineering 162, 106718. doi:10.1016/j.mineng.2020.106718.

Schlegel, M., Stockmann, K., Binder, T., Marquardt, W., 2005. Dynamic optimization using adaptive control vector parameterization. Computers and Chemical Engineering 29, 1731–1751. doi:10.1016/j.compchemeng.2005.02.036.

Shean, B., Hadler, K., Cilliers, J.J., 2017. A flotation control system to optimise performance using peak air recovery. Chemical Engineering Research and Design 117, 57–65. doi:10.1016/j.cherd.2016.10.021.

Shean, B., Hadler, K., Neethling, S., Cilliers, J.J., 2018. A dynamic model for level prediction in aerated tanks. Minerals Engineering 125, 140–149. doi:10.1016/j.mineng.2018.05.030.

Tian, Y., Azhin, M., Luan, X., Liu, F., Dubljevic, S., 2018. Three-Phases Dynamic Modelling of Column Flotation Process. IFAC Proceedings Volumes 51, 99–104. doi:10.1016/j.ifacol.2018.09.399.

Wang, Y., Neethling, S.J., 2006. Simulating realistic froth surfaces 19, 1069–1076. doi:10.1016/j.mineng.2006.03.007.

Zaragoza, R., Herbst, J.A., 1989. Model-based feedforward control scheme for flotation plants. Minerals and metallurgical processing , 177–185.